

Rapid whole-brain resting-state fMRI at 3 T

Citation for published version (APA):

Stirnberg, R., Huijbers, W., Brenner, D., Poser, B. A., Breteler, M., & Stöcker, T. (2017). Rapid whole-brain resting-state fMRI at 3 T: Efficiency-optimized three-dimensional EPI versus repetition time-matched simultaneous-multi-slice EPI. *Neuroimage*, 163, 81-92. <https://doi.org/10.1016/j.neuroimage.2017.08.031>

Document status and date:

Published: 01/12/2017

DOI:

[10.1016/j.neuroimage.2017.08.031](https://doi.org/10.1016/j.neuroimage.2017.08.031)

Document Version:

Publisher's PDF, also known as Version of record

Document license:

Taverne

Please check the document version of this publication:

- A submitted manuscript is the version of the article upon submission and before peer-review. There can be important differences between the submitted version and the official published version of record. People interested in the research are advised to contact the author for the final version of the publication, or visit the DOI to the publisher's website.
- The final author version and the galley proof are versions of the publication after peer review.
- The final published version features the final layout of the paper including the volume, issue and page numbers.

[Link to publication](#)

General rights

Copyright and moral rights for the publications made accessible in the public portal are retained by the authors and/or other copyright owners and it is a condition of accessing publications that users recognise and abide by the legal requirements associated with these rights.

- Users may download and print one copy of any publication from the public portal for the purpose of private study or research.
- You may not further distribute the material or use it for any profit-making activity or commercial gain
- You may freely distribute the URL identifying the publication in the public portal.

If the publication is distributed under the terms of Article 25fa of the Dutch Copyright Act, indicated by the "Taverne" license above, please follow below link for the End User Agreement:

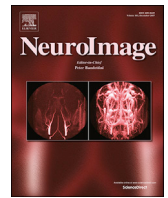
www.umlib.nl/taverne-license

Take down policy

If you believe that this document breaches copyright please contact us at:

repository@maastrichtuniversity.nl

providing details and we will investigate your claim.



Rapid whole-brain resting-state fMRI at 3 T: Efficiency-optimized three-dimensional EPI versus repetition time-matched simultaneous-multi-slice EPI

Rüdiger Stirnberg^{a,*}, Willem Huijbers^{a,b}, Daniel Brenner^a, Benedikt A. Poser^c,
Monique Breteler^a, Tony Stöcker^{a,d}

^a German Center for Neurodegenerative Diseases (DZNE), Bonn, Germany

^b Jheronimus Academy of Data Science, Cognitive Science and Artificial Intelligence, Tilburg University, The Netherlands

^c Faculty of Psychology and Neuroscience, Maastricht University, Maastricht, The Netherlands

^d Department of Physics and Astronomy, University of Bonn, Bonn, Germany

ARTICLE INFO

Keywords:

Echo-planar imaging
3D-EPI
Simultaneous-multi-slice
CAIPIRINHA
Blipped-CAIPI
Physiological noise

ABSTRACT

State-of-the-art simultaneous-multi-slice (SMS-)EPI and 3D-EPI share several properties that benefit functional MRI acquisition. Both sequences employ equivalent parallel imaging undersampling with controlled aliasing to achieve high temporal sampling rates. As a volumetric imaging sequence, 3D-EPI offers additional means of acceleration complementary to 2D-CAIPIRINHA sampling, such as fast water excitation and elliptical sampling. We performed an application-oriented comparison between a tailored, six-fold CAIPIRINHA-accelerated 3D-EPI protocol at 530 ms temporal and 2.4 mm isotropic spatial resolution and an SMS-EPI protocol with identical spatial and temporal resolution for whole-brain resting-state fMRI at 3 T. The latter required eight-fold slice acceleration to compensate for the lack of elliptical sampling and fast water excitation. Both sequences used vendor-supplied on-line image reconstruction. We acquired test/retest resting-state fMRI scans in ten volunteers, with simultaneous acquisition of cardiac and respiration data, subsequently used for optional physiological noise removal (nuisance regression). We found that the 3D-EPI protocol has significantly increased temporal signal-to-noise ratio throughout the brain as compared to the SMS-EPI protocol, especially when employing motion and nuisance regression. Both sequence types reliably identified known functional networks with stronger functional connectivity values for the 3D-EPI protocol. We conclude that the more time-efficient 3D-EPI primarily benefits from reduced parallel imaging noise due to a higher, actual *k*-space sampling density compared to SMS-EPI. The resultant BOLD sensitivity increase makes 3D-EPI a valuable alternative to SMS-EPI for whole-brain fMRI at 3 T, with voxel sizes well below 3 mm isotropic and sampling rates high enough to separate dominant cardiac signals from BOLD signals in the frequency domain.

1. Introduction

Recent advances in undersampled multiband magnetic resonance imaging (MRI) (Larkman et al., 2001) and increasing availability of state-of-the-art simultaneous-multi-slice echo-planar imaging (SMS-EPI) (Setsompop et al., 2012) has made application of three- to eight-fold slice-accelerated whole-brain diffusion MRI and functional MRI (fMRI) feasible on a routine basis (Breteler et al., 2014; Miller et al., 2016; Smith et al., 2013; Sotiropoulos et al., 2013; Uğurbil et al., 2013). As opposed to spin-echo-based diffusion MRI, which benefits from the “snap shot” character of SMS-EPI, gradient-echo-based fMRI does not suffer from

severe sub-millimeter motion artifacts, if image acquisition is distributed across multiple shots. Three-dimensional echo planar imaging (3D-EPI) (Poser et al., 2010) with controlled aliasing in volumetric imaging (2D-CAIPIRINHA) (Breuer et al., 2006) has therefore been suggested (e.g. (Narsude et al., 2013; Narsude et al., 2014b; Poser et al., 2013, 2014; Stirnberg et al., 2016b)) as a potential alternative to SMS-EPI with blipped controlled aliasing in parallel imaging (blipped-CAIPI) (Setsompop et al., 2012). Particularly at ultra-high fields 3D-EPI has the potential to achieve high acceleration factors at high spatial resolutions without exceeding specific-absorption-rate (SAR) or radiofrequency (RF) peak power limits (Poser et al., 2010; Stirnberg et al., 2013). This is due

* Corresponding author. Sigmund-Freud-Str. 27, D-53127, Bonn, Germany.
E-mail address: ruediger.stirnberg@dzne.de (R. Stirnberg).

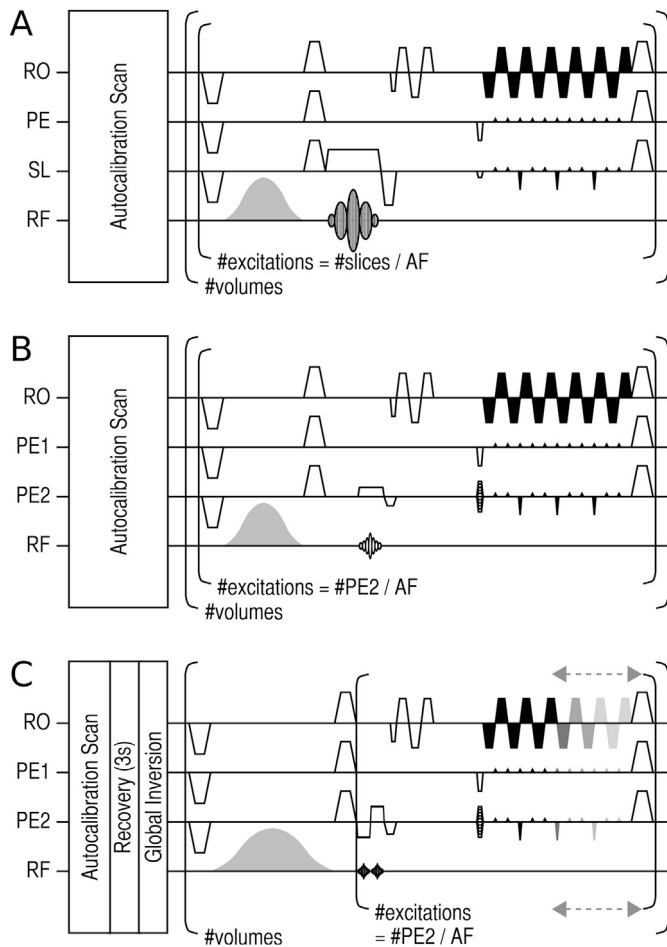


Fig. 1. Sequence diagrams of a generic SMS-EPI (A, multiband excitation), a corresponding 3D-EPI (B, slab-selective excitation) and the efficiency-optimized 3D-EPI (C, slab-selective water excitation). For each volume acquisition, the inner loop (i.e. optional CHESSE fat-saturation, excitation, phase correction scans, EPI readout and spoiler gradients) runs several times, which defines the minimum volume TR. The number of excitations per volume is defined by the final number of reconstructed slices ($\#slices$) or PE2 steps ($\#PE2$) divided by the acceleration factor, AF (slice acceleration factor or PE2 undersampling factor, respectively). The Gaussian CHESSE RF pulses in (A) and (B) and the adiabatic SPAIR RF pulse in (C) (gray) are fat selective. The EPI color gradient and the dashed arrows in (C) indicate that the ETL, and hence the TR across excitations, is variable.

to much simpler “singleband” spatially- or frequency-selective excitation pulses (Störnberg et al., 2016a) or composite pulses that even allow for relatively simple parallel transmission field homogenization (Tse et al., 2016).

3D-EPI and SMS-EPI share several properties. For instance, both suffer from typical, susceptibility-induced geometric distortions only along the primary phase encode (PE) direction, as opposed to single-shot echo-volumar imaging (EVI) (Mansfield et al., 1989). As a matter of fact, blipped-CAIPI SMS-EPI and 2D-CAIPIRINHA 3D-EPI are equivalent under a generalized 3D Fourier description (Zahneisen et al., 2014) and can be reconstructed with identical g-factor penalties (Zahneisen et al., 2015). A thorough proof-of-concept characterization of SMS-EPI and 3D-EPI across a range of matching sequence parameters, in particular with regard to physiological noise, is of great scientific value. However, a stringent comparison is not as trivial in practice. Even if matching pulse sequence and on-line image reconstruction implementations were available, certain time-critical sequence aspects, such as the excitation pulse duration, cannot reasonably be equalized without unfairly penalizing one sequence type. Furthermore, 3D-EPI exclusively offers complementary acceleration techniques not based on parallel imaging principles (Poser et al., 2010; Störnberg et al., 2014, 2016a), which are

impossible to account for in such a hypothetical comparison.

This work, instead, aims at an application-oriented comparison of SMS-EPI and 3D-EPI at 3 T. The use of readily available on-line image reconstruction is of particular importance for actual feasibility and high-throughput utilization, e.g. for clinical or population-based studies (Breteler et al., 2014; Miller et al., 2016). The SMS- and 3D-EPI protocols investigated here are individually optimized for fast whole-brain fMRI with equal spatial and temporal resolution and otherwise – to the greatest possible extent – matching parameters. As a precondition, the imaging rate shall be fast enough to preclude aliasing of high cardiac frequencies (60–100 beats per minute) into typically considered BOLD frequencies (0.01–0.08 Hz).

2. Methods

All experiments were performed on a 3 T MAGNETOM Prisma scanner (Siemens Healthcare, Erlangen, Germany, software baseline VE11C) equipped with a nominal 80 mT/m and 200 T/m/s gradient system and a 64 channel head/neck receive array, of which the 52 head elements were utilized.

2.1. Custom 3D-EPI sequence

A time-optimized 3D-EPI sequence was developed in-house, which allowed for the introduction and combination of several dedicated techniques for enhancement of the sampling efficiency, as explained below.

2.1.1. 2D-CAIPIRINHA

Following several recent publications (Narsude et al., 2016, 2013; Poser et al., 2013; Zahneisen et al., 2015), we implemented an echo-planar 2D-CAIPIRINHA sampling scheme that minimizes the number of excitations per volume repetition time (TR). Following excitation, the k -space trajectory traverses as many secondary PE locations (PE2) as possible under the constraint of a constant bandwidth along the primary PE direction (PE1) and a virtually infinite bandwidth along PE2 (steady progression along PE1, as opposed to single-shot EVI or 3D-EPI with reduced number of segments without 2D-CAIPIRINHA (Narsude et al., 2014a)). Analogous to blipped-CAIPI SMS-EPI (Setsompop et al., 2012), this requires blipped gradients along both PE1 and PE2, as illustrated by the sequence diagrams in Fig. 1 (A,B). The inset in Fig. 2(F) demonstrates such a k -space sampling scheme on the example of a $R = 1 \times 6^{(2)}$ CAIPIRINHA pattern, where the superscript denotes the CAIPIRINHA shift in units of the PE2 increment (Breuer et al., 2006). For image reconstruction we utilize a generic, vendor-provided 2D-GRAPPA (Griswold et al., 2002) implementation compatible with 2D-CAIPIRINHA sampling, which we refer to as CAIPIRINHA reconstruction.

2.1.2. Variable echo train lengths

The sampling scheme is extended by two elliptical sampling options that restrict the actually sampled (PE1,PE2) k -space points to either an “elliptical” or “semi-elliptical” subset, whereby the radius is determined by the nominal desired image resolution (Bernstein et al., 2001). Such 2D k -space masking implies that the complete image is defined along two PE directions; a corresponding technique is thus, to the best of our knowledge, not available to SMS-EPI. Applied to 3D-EPI, skipping of k -space points outside the elliptical mask results in variable echo train lengths (vETL) across excitations, which can be used to increase imaging speed (Störnberg et al., 2014). The fraction of k -space outside a full elliptical mask corresponds to $1 - \pi(0.5)^2 \approx 21\%$ of the total rectilinear k -space volume. Accordingly, “elliptical” and “semi-elliptical” sampling can theoretically save up to 20% and 10% readout time, respectively. Skipping only points at the end of a given EPI echo train results in a variable TR across excitations (cf. Fig. 2 B), whereas skipping also points at the beginning of the echo train additionally results in variable TE (cf. Fig. 2

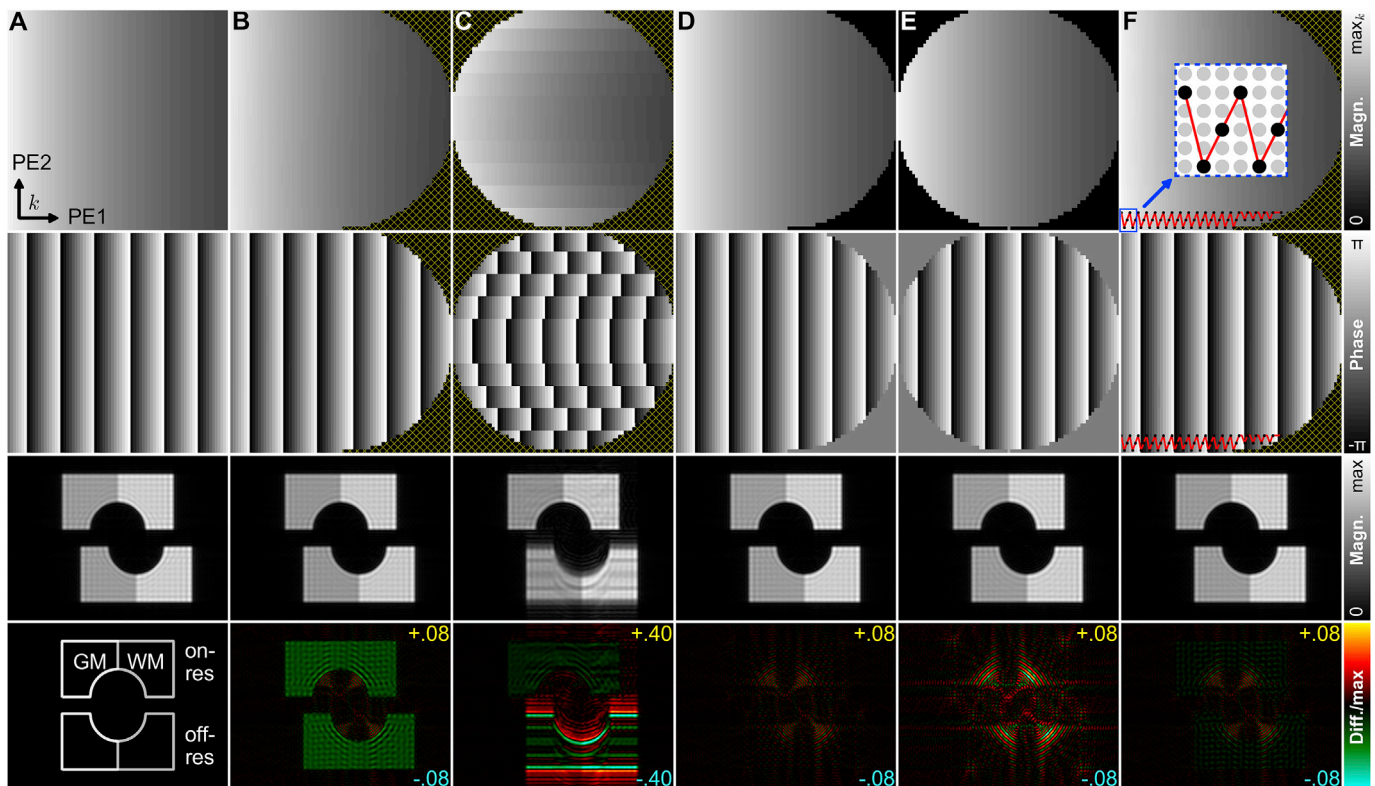


Fig. 2. Different vETL and masking approaches demonstrated on simulated 3D-EPI images. Bottom left: numerical phantom; top rows: complex modulation transfer function for off-resonant GM (hatched = skipped); bottom rows: corresponding images and relative difference images with respect to full sampling (A). Color scaling is constant across columns (except relative difference in C). Semi-elliptical vETL (B) and conventional k -space sampling (A) lead to almost identical images including off-resonance pixel shifts, aside from a global signal reduction of approximately 3% due to a reduced average TR across excitations. Variable TE (C) leads to severe off-resonance artifacts in addition to a circular PSF. (D,E) demonstrate the pure masking effects, without vETL, on the PSF. (F) corresponds to the fast 3D-EPI protocol adopted in this work, including SPAIR fat suppression. The red line in (F) indicates the k -space trajectory of the first echo train per volume. The inset in (F) illustrates the $1 \times 6^{(2)}$ CAIPIRINHA sampling pattern (black dots). The relative difference images of (D) and (F) indicate minimal deviation from the fully sampled reference.

C). Variable TR (with constant TE) across excitations has negligible effect on the point spread function (PSF) since, first, the resulting periodic magnitude variations along PE2 are smooth and small (0.3% coefficient of variation in Fig. 2 B), and second, only strongly decayed T_2^* -weighted signals outside the elliptical mask are skipped. The corresponding spatial frequencies with minimal T_2^* -weighting on the opposite part of k -space are not skipped (cf. Fig. 2 D). However, the reduction of the average TR across excitations also causes a small signal decrease, as demonstrated by the relative difference image in Fig. 2(B). Variable TE, on the other hand, can lead to: first, a reduced BOLD contrast due to an emphasized contribution of short TE signals (e.g. at $k_{PE1} = 0$), second, to severe off-resonance artifacts due to phase discontinuities (cf. Fig. 2 C), and third, to a circular point spread function due to the elliptical mask (cf. Fig. 2 E). The numerical phantom images in Fig. 2 have been simulated using the extended phase graph approach (Hennig, 1991a, 1991b) for realistic k -space signal envelopes along PE2, combined with a mono-exponential T_2^* decay/linear phase accrual along PE1. Approximate white matter (WM) and gray matter (GM) relaxation times at 3 T ($T_1/T_2/T_2^* = 800/80/35$ and $1500/80/35$ ms, respectively; 0 and 150 Hz off-resonant) and imaging parameters according to the fast 3D-EPI protocol used below have been assumed. Based on the simulations it was decided to only pursue the semi-elliptical vETL approach.

2.1.3. Rapid water excitation and fat-selective inversion recovery

Robust fat suppression in EPI is typically achieved by means of chemical shift selective fat excitation (CHESS (Haase et al., 1985)) followed by gradient crushers prior to each excitation per volume. The default duration of a single fat saturation module in our vendor-supplied EPI sequences is about 12 ms. In a typical BOLD imaging scenario (TE = 30–35 ms, readout duration 30 ms) this means that about 20% of

the total sequence are not spent on signal acquisition. Hence, more efficient schemes for avoiding fat contributions are highly desirable. Particularly rapid narrowband water excitation (WE) can be performed using the simplest $1\bar{1}$ -type of binomial excitation consisting of only two sub-pulses, which we refer to as binomial-11 WE (Hore, 1983). Note that the included free-precession period (~ 1.2 ms at 3 T) requires relatively short sub-pulses, which are in practice only feasible with “singleband” excitation. In addition to increased imaging efficiency (TR reduction on the order of 20%), binomial-11 WE has been shown to avoid the significant signal-to-noise ratio (SNR) reduction in 3D-EPI that otherwise results from the frequent application of high-energy CHESS pulses (Störnberg et al., 2016a). More elaborate, longer composite pulses, such as binomial-121 WE, could be used, if greater robustness against main field inhomogeneities is required. Such pulses are, however, more restrictive with regard to the minimum possible TE.

The targeted short TR facilitates an alternative means, complementary to binomial-11 WE, by utilizing the short T_1 of fat, which is robust against an insufficient or drifting shim. A spectral adiabatic inversion recovery (SPAIR) module was implemented, as a fat-selective, adiabatic variant of short inversion time inversion recovery (STIR) (Bydder et al., 1985). One SPAIR module of approximately 29 ms duration runs only prior to the first WE per volume TR (cf. Fig. 1 C), such that the longitudinal fat magnetization is approximately nulled at the excitation time corresponding to the $k_{PE2} = 0$ trajectory. Hence, residually excited fat magnetization is as small as possible. At 3 T the required duration from inversion to the WE preceding the $k_{PE2} = 0$ trajectory is in the order of 200–300 ms. As a secondary effect, the longitudinal relaxation period between the last and the first excitation of successive volume acquisitions is prolonged. According to numerical phantom simulations (cf. Fig. 2 B and F), SPAIR may thus lead to a beneficial signal increase without

Table 1
Summary of SMS- and 3D-EPI sequence parameters.

Parameter	SMS-EPI	3D-EPI
Matrix size	80 × 80 × 56	80 × 80 × 60
Voxel size [mm ³]	2.4 × 2.4 × 2.4	2.4 × 2.4 × 2.4
Nominal FOV [mm ³]	192 × 192 × 134.4	192 × 192 × 144.0
Actual FOV [mm ³]	192 × 192 × 134.4	192 × 192 × 134.4
Parallel imaging	slice acceleration factor: 8	k-space undersampling: 1 × 6
Controlled aliasing	blipped-CAIPI shift: FOV/ 3	2D-CAIPIRINHA shift: 2Δk
Calibration data	56 slices × 36 PE	36 PE1 × 36 PE2
Reconstruction algorithm	Slice-GRAPPA	2D-GRAPPA
Readout bandwidth [Hz/pixel]	2604	2604
Echo spacing [ms]	0.55	0.55
Echo train lengths	{80, 80, 80, 80, 80, 80, 80}	{58, 70, 76, 79, 80, 80, 80, 77, 71, 64}
Fat suppression	7 × CHES fat sat.	1 × SPAIR, 10 × binomial-11 WE
TE [ms]	30	30
TR [ms]	530	530
TI _n [ms]	–	220 + n · TR
Nominal flip angle [°]	45	16
Measurements (retained)	1152 (1133)	1152 (1133)
TA (retained) [min:sec]	10:19 (10:00)	10:25 (10:00)

adversely affecting the PSF.

2.2. Product SMS-EPI sequence

We use the vendor-supplied state-of-the-art SMS-EPI sequence, which is based on the recently developed blipped-CAIPI technique and employs slice-GRAPPA image reconstruction (Setsompop et al., 2012) with slice leakage suppression (Cauley et al., 2014). The PE field-of-view (FOV) shift and the excitation pulse are automatically set depending on imaging parameters (Xu et al., 2013).

2.3. Data acquisition

Ten healthy young subjects (age 24±3 years, 5 female) attended two scanning sessions after providing informed consent in accordance with local institutional review board regulations. In order to assess test/retest reliability each session included both SMS-EPI and 3D-EPI resting-state fMRI scans. Between sessions the subjects left the scanner for approximately one hour. The acquisition order of SMS- and 3D-EPI scans was pseudo-randomized across subjects. To preclude variable main field shims affecting image quality, the shim currents were automatically adjusted only prior to the first EPI scan per session and kept unchanged thereafter. Respiration and heart beat were recorded synchronously with the EPI scans using the vendor-provided respiration belt and plethysmograph. During the first session a 0.8 mm isotropic sagittal T₁-weighted scan was acquired for anatomical reference (MP-RAGE (Mugler and Brookeman, 1990) using elliptical sampling and 2D-CAIPIRINHA acceleration (Brenner et al., 2014), $R = 1 \times 3^{(1)}$, TI/TE/TR = 1100 ms/5 ms/2560 ms, 7° flip angle, TA = 3:43 min). The default receive inhomogeneity correction, which utilizes an initial body-coil reference pre-scan, was enabled for all scans. For the sake of brevity, and if applicable, the two EPI protocols are referred to as “3D” and “SMS” in the remainder of this work.

A (192 mm)² axial FOV with conventional anterior–posterior PE

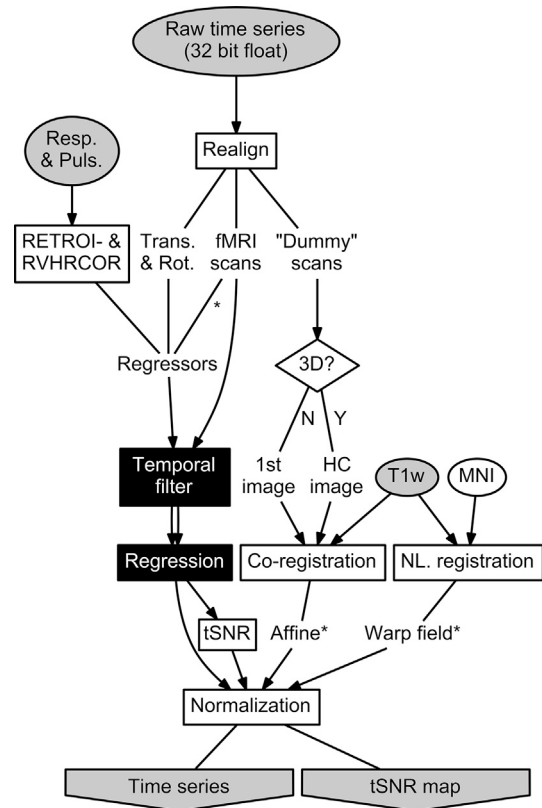


Fig. 3. Schematic representation of the nipype preprocessing pipeline. Subject-specific input and output is indicated by gray background color. Nodes with black background color are executed with several combinations in parallel (temporal filter: high pass/band pass; GLM regression: none/motion/motion and nuisance). The asterisks indicate that the inverse of affine and warp field are also utilized to initially extract nuisance regressors from well defined masks in individual subject space. Note that no explicit smoothing is involved and that normalization is performed as a very final step.

direction and (2.4 mm)² in-plane resolution was used for both 3D and SMS. The slice orientation was tilted by additional 6° to the coronal plane with respect to the automatic AC-PC-like FOV alignment featured by the scanner software. Detailed sequence parameters are listed in Table 1. The 3D protocol applied slab-selective binomial-11 WE using apodized sinc sub-pulses of 0.8 ms duration with a bandwidth-time-product of 35, yielding an approximate slab thickness of 134.4 mm at 2.4 mm slice resolution. Folding of the side bands was prevented by extending the nominal slice-FOV to 144 mm (60 slices, i.e. two slices discarded on either side of the slab). The SMS-EPI protocol acquired a 134.4 mm stack of 56 slices (2.4 mm nominal slice thickness, no gaps). In both cases the slice number had to be an integer multiple of the slice acceleration factor.

The 3D-EPI protocol employed semi-elliptical vETL and binomial-11 WE combined with SPAIR fat suppression and thus required only $R = 1 \times 6^{(2)}$ CAIPIRINHA sampling (cf. Fig. 2 F) to achieve a volume TR of $TR_{\min} = 530$ ms at TE = 30 ms. Slice partial Fourier sampling was specifically not employed to avoid potentially increased signal drop outs in regions of large magnetic susceptibility gradients. Approximating the Ernst angle in GM at 3 T, the effective binomial-11 WE flip angle was set to 16° (8° for each sub-pulse). With otherwise matching sequence parameters, but using CHES fat saturation and automatically prepared multiband excitation (five-lobe apodized sinc envelope of 6.8 ms duration), SMS-EPI required a slice acceleration factor of eight (FOV/3 PE shift) to achieve the same TR (the actual TR_{\min} with a slice acceleration factor of seven and eight was 560 ms and 500 ms, respectively). A corresponding Ernst angle of 45° was adopted to maximize GM signal.

The autocalibration scan (ACS) for the vendor-supplied default CAIPIRINHA reconstruction was acquired prior to the 3D-EPI imaging scans as a fully sampled central 36 × 36 k-space subset. To minimize the

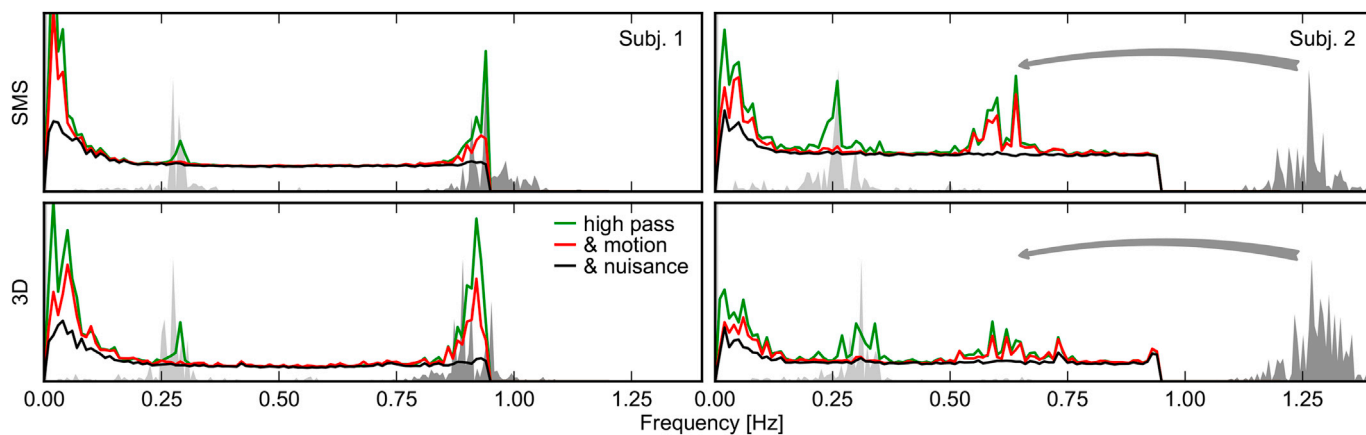


Fig. 4. Example whole-brain PSD with SMS-EPI (top) and 3D-EPI (bottom) using high pass temporal filtering only (green), additional motion regression (red), and additional motion & nuisance regression (black). The gray arrows indicate the aliasing of the fundamental cardiac frequencies for the second example subject. The PSDs of the raw plethysmograph (dark gray) and respiration belt measurements (light gray) are not aliased due to a high sampling rate of 400 Hz.

influence of physiologically induced data inconsistencies and phase errors, a line-by-line fast low angle shot (FLASH) approach, using isolated readout gradient and excitation pulses identical to the ones used for the subsequent EPI acquisition, was adopted with a flip angle of 3° (Ivanov et al., 2015; Talagala et al., 2016). Following ACS, a short longitudinal recovery period of 3 s and a single, global adiabatic inversion pulse are introduced to generate a rich inversion recovery (IR) T_1 contrast while the subsequent “dummy” scans are acquired (cf. Fig. 1 C). For SMS-EPI 36 central PE lines of the complete set of 56 slices were acquired as ACS data for the vendor-supplied slice-GRAPPA reconstruction. Since only slice acceleration, and no undersampling along the PE direction was performed, the recently proposed fast low-angle excitation echo-planar technique (FLEET) for SMS-EPI (Bhat et al., 2014; Blazejewska et al., 2017) corresponded to a single-shot EPI acquisition. All preparation scans, 19 stored “dummy” volumes (10 s) and 1133 “steady state” volumes (10 min) resulted in total acquisition times (TA) of 10:25 (3D) and 10:19 (SMS) minutes. An additional, short SMS-EPI scan, using a slice acceleration factor of six, was acquired only for the purpose of computing corresponding tSNR maps (280 vol, TA = 3:22 min). To keep changes minimal, all protocol parameters were identical to the resting state SMS-EPI protocol, except for the number of slices (60) and the volume TR (690 ms = TR_{\min}). Accordingly, steady-state signal increases of approximately 12.7%/8.1% can be expected in GM/WM compared to the resting state SMS-EPI protocol.

2.4. Data preprocessing

The EPI time series were preprocessed within the nipy python framework (Gorgolewski et al., 2011) (version 0.11.0) as outlined in a simplified form in Fig. 3. Retrospective motion correction (realignment) to the first of the 1133 “steady state” volumes, linear co-registration to the T_1 -weighted image and non-linear registration to a 2 mm T_1 -weighted Montreal Neurological Institute (MNI) standard template were performed using FSL’s MCFLIRT, FLIRT (BET) and FNIRT interfaces (version 5.0), respectively (Jenkinson et al., 2012). Linear co-registration was aided by a “high-contrast” EPI reference image obtained from the “dummy” volumes as either the very first acquired SMS image, or a high- T_1 -contrast 3D image. Adapting the approach from (O’Brien et al., 2014), the latter is computed from the first three IR “dummy” images, $I_{0,1,2}$, and the mean steady state image, μ , according to Eq. (1), where the constant $\eta = 4095 \geq I_{0,1,2}$ is used to suppress noise in air regions.

$$HC = \max \left\{ 0, \frac{I_1 + I_2 - I_0 - 2\eta}{2(\mu + \eta)} + 1 \right\} \in [0, 1] \quad (1)$$

In order to generate three time-courses of mean WM, mean

cerebrospinal fluid and mean global brain signal for later nuisance regression, the inverse of the normalization transform (affine and warp field) was used to define corresponding masks in subject space based on the 2 mm Harvard-Oxford subcortical MNI atlas provided with FSL (indicated by asterisks in Fig. 3). The WM mask was eroded in three iterations to eliminate GM voxels prior to subject space transformation (cf. Fig. 5 top, right). 14 additional nuisance regressors were derived from the external measurement units using in-house python implementations of the RETROICOR method with up to second-order harmonics (Glover et al., 2000) and the RVHRCOR (Chang et al., 2009) method using cardiac and respiratory response functions as defined by Eq. (5) in Chang et al. (2009) and Eq. (3) in Birm et al. (2008), respectively. 24 motion regressors were derived from the realignment parameters (3 translation, 3 rotation, 6 derivatives, 12 squared (Power et al., 2014)).

Temporal high pass (HP) or band pass (BP) filtering of the EPI time series was performed using a second-order digital butterworth filter (cut-off frequencies HP: 0.01 Hz, BP: 0.01 Hz and 0.08 Hz) applied using the forward-backward `scipy.signal.filtfilt` function (Oliphant, 2007). Motion and nuisance regression were performed simultaneously following temporal filtering using the fMRI general linear model (GLM) implementation within the nipy library (Millman and Brett, 2007). As recommended in Hallquist et al. (2013), the identical temporal filter as used for the EPI time series was applied to the GLM regressor array before being passed to the regression node. To compare the effects of temporal filters and nuisance regressors on SMS and 3D data, the respective nodes were performed with all combinations given by [HP; BP] \times [no GLM regressors; 24 motion regressors; 24 motion + 17 nuisance regressors]. Following GLM regression the “clean” time series was used to compute voxel-wise tSNR and the mean brain power spectrum density (PSD). The time series and the tSNR map were both finally normalized using FNIRT. Note that no explicit smoothing was applied.

2.5. Temporal signal-to-noise ratio analysis

For visualization purposes, we averaged the normalized tSNR maps of the first session across subjects for each combination of temporal filter and GLM regression. For quantitative tSNR analysis, the median values of several regions-of-interest (ROIs) were extracted from the corresponding native tSNR maps of each subject and compared by sequence type using a two-sided paired T-test (`scipy.stats.ttest_rel`). Just as the image-based nuisance regressor masks, these ROIs were first defined based on the 2 mm Harvard-Oxford subcortical MNI atlas (cortical and subcortical GM) and the 2 mm Cerebellum atlas (cerebellar GM) provided with FSL, then eroded to minimize potential misclassification (cerebellar/subcortical/cortical GM: 1/1/2 iterations, cf. Fig. 5 top, right) and finally transformed to individual subject space.

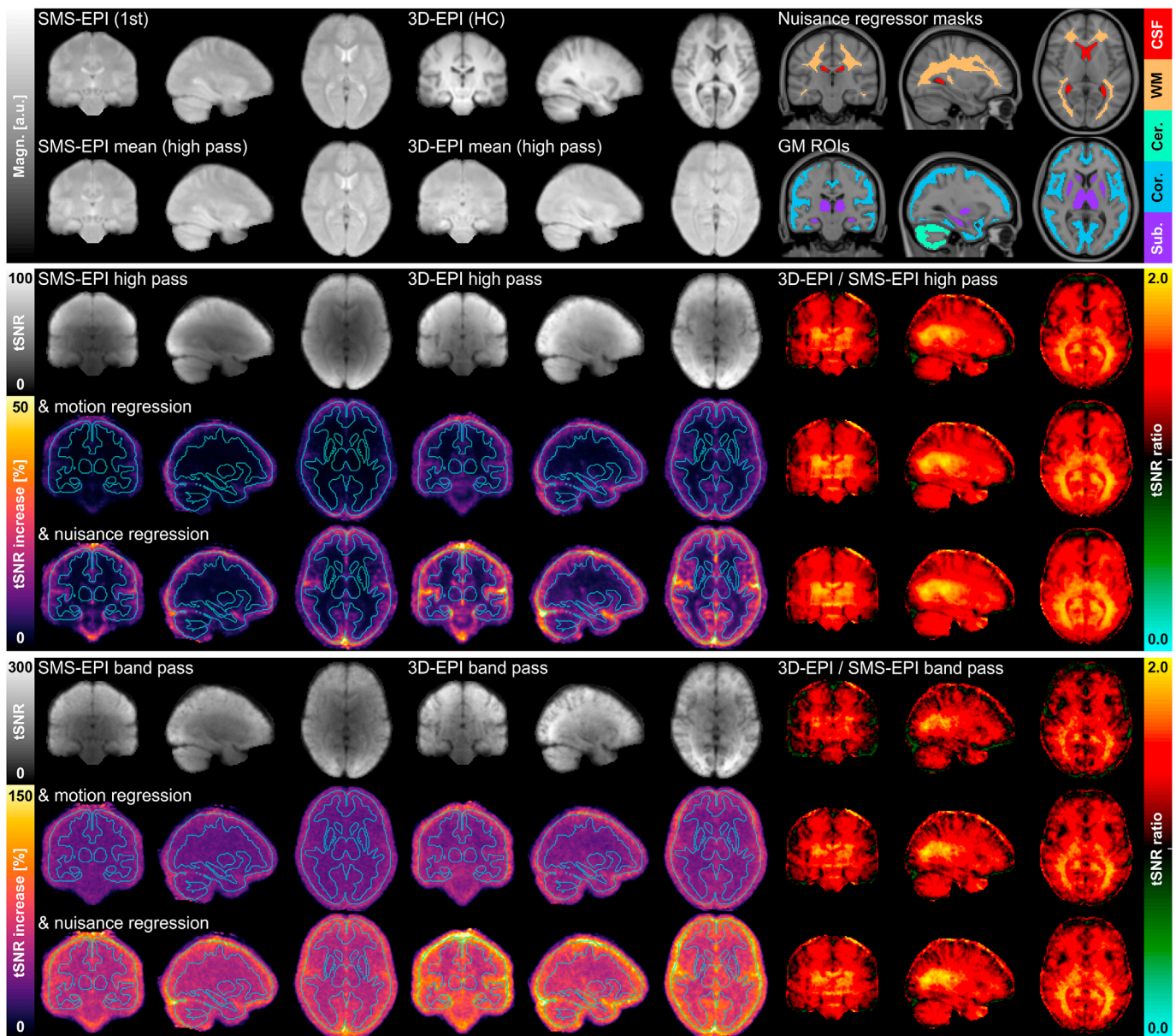


Fig. 5. Comparison of group mean maps with SMS-EPI (left) and 3D-EPI (center). Top panel: “high-contrast” reference image and time series mean. Middle and bottom panel: group mean tSNR maps for temporal high pass and temporal band pass filtered data and the ratio of tSNR with 3D-EPI and SMS-EPI (right). Within each panel the improvement by motion regression (middle row) or motion and nuisance regression (bottom row) in addition to temporal filtering is displayed as a spatial map of relative tSNR increase. The superimposed GM contours, serving as visual guides, correspond to the original, non-eroded GM masks. The masks displayed in the top panel (right) correspond to the eroded WM and CSF masks used to define nuisance regressors, and to the eroded cortical, subcortical and cerebellar GM masks used for the ROI analysis.

2.6. Functional connectivity analysis

Functional connectivity estimates were derived from the normalized HP time series, after motion and nuisance regression, using a template based rotation (TBR) method (Schultz et al., 2014). The TBR method works similar to the dual-regression approach in independent component analysis (ICA) (Beckmann and Smith, 2005), although it differs in several details. TBR estimates weights of predefined templates (i.e. prediction of templates as a linear combination of functional time courses) instead of estimating the weights of independent components (i.e. prediction of functional time courses as a linear combination of predefined templates). We used the “default” templates derived from a data set of 675 subjects as previously described (Schultz et al., 2014). The TBR method effectively regresses all voxels at each time point for an individual subject onto the matrix of all voxels for each template in the reference dataset. The resulting beta-weights are estimated for each template and reflect the

unique variance attributable to a time point in the subject’s data (factor loading). These voxel-wise factor loadings are equivalent to voxel-wise component loadings in an ICA. Similar to ICA, TBR does not suffer from autocorrelations by a seed region. The TBR templates also consist of multiple regions distributed across the brain that help avoid this form of over-fitting to the time-course of a single region. The comparison between TBR, ICA and seed-based approaches has been previously published (Schultz et al., 2014). One advantage of the TBR method is that individual connectivity estimates can be obtained for predefined networks in relation to an independent reference dataset. Thus, using out-of-sample templates makes it easy to compare results from different sequences. Using TBR, we estimated the factor loadings in each voxel for each network ($F = 20$), subject ($n = 10$), session (test/retest) and sequence type (SMS/3D).

We conducted ROI and whole-brain voxel-wise group analyses on the TBR connectivity maps. First, we defined the ROIs based on previous

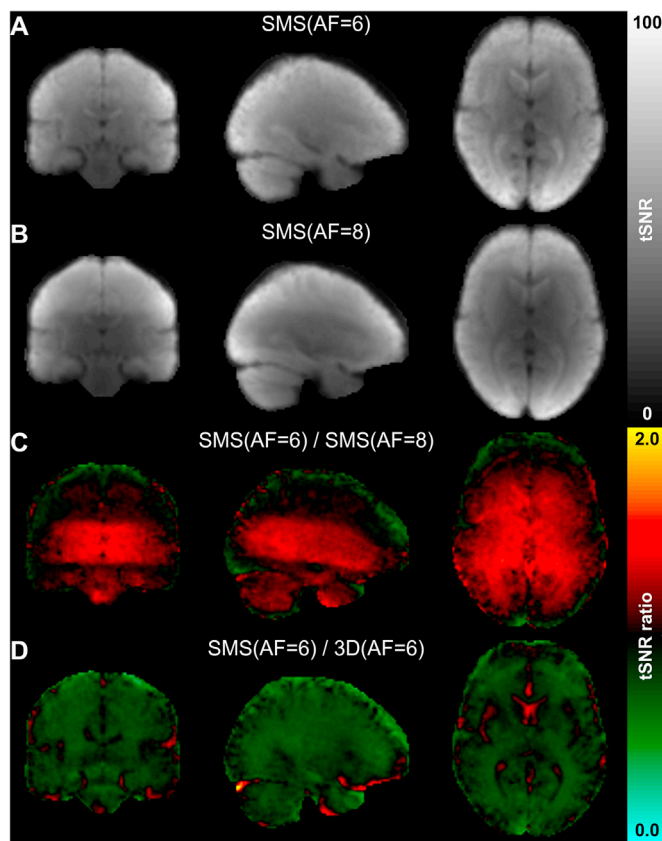


Fig. 6. Group mean tSNR maps of six-fold (A) and eight-fold (B) accelerated SMS-EPI data following temporal high pass filtering. The corresponding tSNR ratio map is displayed in (C). An additional tSNR ratio map of six-fold accelerated SMS-EPI and 3D-EPI is shown in (D).

work (Van Dijk et al., 2010) using the mean of a 5 mm sphere from a-priori coordinates in MNI standard space: the motor network connectivity estimates (TBR: Factor-03) were extracted from the left [$MNI(x, y, z) = -36, -25, 57$] and right [$MNI(x, y, z) = -36, -25, 57$] motor cortex, the default-network connectivity estimates (TBR: Factor-02) from the posterior cingulate cortex [$MNI(x, y, z) = 0, -53, 25$] and medial prefrontal cortex [$MNI(x, y, z) = 0, 52, -6$] and visual network connectivity estimates (TBR: Factor-04) from the left [$MNI(x, y, z) = -30, -88, 0$] and right [$MNI(x, y, z) = 30, -88, 0$] visual cortex. The estimates were then averaged across both ROIs to obtain a single connectivity estimate per network. Next, we conducted repeated measure ANOVA including a factor for sequence (SMS/3D), session (test/retest) and the interaction term. For whole-brain connectivity analyses we used SPM12 (<http://www.fil.ion.ucl.ac.uk/spm/>) in combination with GLM_Flex (<http://mrtools.mgh.harvard.edu>). Statistical group maps were projected to the cortical surface using FreeSurfer (v5.1) via a standard MNI to the FreeSurfer average template transformation. Finally, we calculated the voxel-wise intraclass correlation coefficient (ICC(2,1)) to visualize test/retest reliability for connectivity estimates in each voxel for SMS and 3D separately (Shrout and Fleiss, 1979, Bennett and Miller (2010)). The group ICC maps were smoothed with a 8 mm FWHM kernel for visualization purposes and projected to the cortical surface.

3. Results

Fig. 4 displays the mean brain PSD of two example subjects obtained from SMS and 3D data of the same session for increasing degrees of data “cleaning”. To identify the origins of the physiological noise peaks, the PSDs of the external respiratory and cardiac measurements sampled at

400 Hz are added in light and dark gray color. While both subjects had similar respiratory frequencies, subject two had a relatively high heart rate between 70 and 80 beats per minute (~ 1.17 – 1.33 Hz), which is not yet considered tachycardia. Owing to the high Nyquist frequency ($TR = 0.53$ s corresponds to ~ 0.943 Hz), the first alias signals (~ 0.55 – 0.72 Hz) do not overlap with the BOLD frequencies.

3.1. Temporal signal-to-noise ratio

The top panel of Fig. 5 displays group mean maps of the anatomical reference image involved in the preprocessing co-registration step (first row) and of the time series mean image (second row). The remaining panels show absolute group mean tSNR maps for SMS- and 3D-EPI in case of HP (middle) and BP filtering (bottom). To identify particular regions of improvement we have displayed maps of relative tSNR increase by motion regression and by motion and nuisance regression with respect to the corresponding tSNR maps with temporal filtering only. Overall, the highest increases are observed in cortical GM for both SMS and 3D. For each combination of temporal filter and regression, the explicit tSNR ratio map (3D/SMS) is shown on the right. A small number of voxels in frontotemporal and lower occipital brain areas show ratios barely below 1.0 without motion and/or nuisance regression. A clear majority of voxels, however, shows ratios well above 1.0, in particular in CSF (about 1.5) and central WM areas (about 2.0). A corresponding tSNR ratio map of six-fold vs. eight-fold accelerated SMS-EPI, as displayed in Fig. 6 C, shows a similar tSNR benefit in the center of the brain. However, the maximum ratio is in the order of 1.5 irrespective of the tissue type, and the geometric pattern is more sharply defined across the inferior–superior direction. Such a pattern is absent in the corresponding tSNR ratio map of SMS-EPI vs. 3D-EPI, both six-fold accelerated (cf. Fig. 6 D), which exhibits increased values in CSF (about 1.5), decreased values in WM throughout the brain (about 0.8) and a ratio about 1.0 in GM.

Box plots for cerebellar, subcortical and cortical GM using all investigated temporal filtering and GLM regression combinations are shown in Fig. 7. Group mean values, additionally plotted as colored dots, match the group median values well and indicate, across all ROIs, a clear tSNR benefit of 3D (blue) over SMS (red). The symbol “#” marks the only tSNR difference between 3D and SMS found to be statistically nonsignificant. All other differences were found highly significant ($p < 0.001$). The numbers in the center and right panels (B,C,E,F) give an estimate of the relative group mean tSNR increase by GLM regression in addition to temporal filtering. Table 2 states all group mean tSNR values and their ratios (3D:SMS) including relative standard errors (in parentheses) as well as the explicit T and p values from the paired T-tests. The letters “M” and “N” stand for motion and nuisance regression. According to Fig. 7 and Table 2 the largest improvements by motion and nuisance regression are observed in cortical GM for both sequences (SMS/3D) and temporal filters (HP/BP). Notably, in case of HP filtering, 3D benefits about twice as much from motion and nuisance regression ($\sim 20\%$ increase to 64 ± 2) as SMS ($\sim 10\%$ increase to 51 ± 2). In case of BP filtering, cortical GM tSNR is increased by about 90% to 241 ± 10 (3D) compared to approximately 70% increase to 200 ± 10 (SMS). A similar trend is observed in cerebellar and subcortical GM for both temporal filters.

3.2. Functional connectivity

Fig. 8 shows the results of the ROI functional connectivity analysis in the motor, default and visual network. In the motor network, we found greater connectivity for 3D [$F(1, 27) = 18.0, p < 0.001$], while we found no effects of session (test/retest) [$F(1, 27) = 0.67, p = 0.42$] or interaction [$F(1, 27) = 0.66, p = 0.42$]. In the default-network, we also found greater connectivity for 3D [$F(1, 27) = 47.1, p < 0.001$] and no effect of session [$F(1, 27) = 2.00, p = 0.17$]. However, we also observed an interaction [$F(1, 27) = 6.01, p = 0.021$], indicating the main effect of sequence type should not be interpreted. Finally, in the visual network, we found greater connectivity for 3D [$F(1, 27) = 20.8, p < 0.001$], while

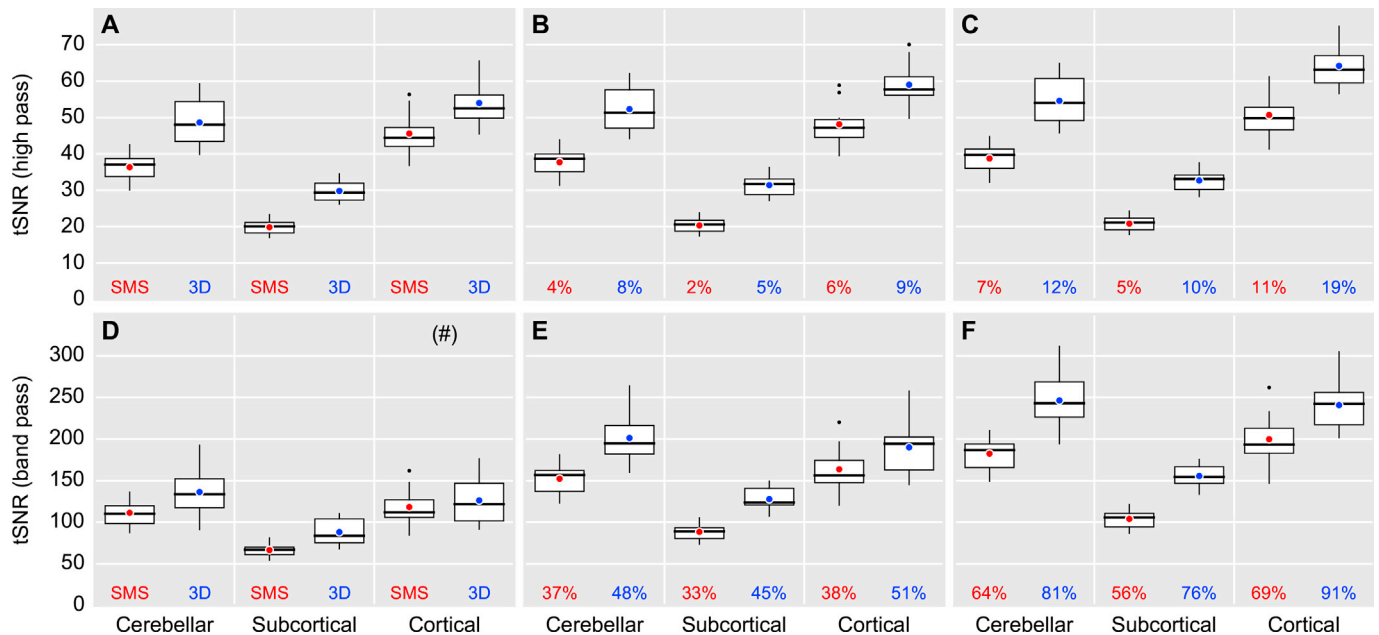


Fig. 7. Quantitative group analysis of the median tSNR in cerebellar, subcortical and cortical GM. The top and bottom panels reflect temporal high pass (A–C) and temporal band pass filtered data (D–F). Numbers at the bottom indicate the relative tSNR increase of the group mean (colored dots) by motion regression (B,E), and by motion and nuisance regression (C,F) relative to the group mean with temporal filtering only (A,D). All differences between SMS-EPI and 3D-EPI (except #) are highly significant ($p < 0.001$).

we found no effects of session [$F(1, 27) = 1.88, p = 0.18$] or interaction [$F(1, 27) = 0.00, p = 0.97$]. Fig. 9 shows whole-brain connectivity maps across both sessions separately for SMS and 3D (left) and the corresponding ICC maps (right).

4. Discussion

We have proposed several modifications to a 3D-EPI acquisition scheme that result in greater SNR and sampling efficiency than typically applied state-of-the-art SMS-EPI. Specifically, the time efficiency was achieved by use of fast water excitation and semi-elliptical sampling with variable echo train lengths. No slice partial Fourier sampling was employed to maintain comparability with SMS-EPI with respect to signal drop outs and actual image resolution. Both sequences utilized equivalent parallel imaging acceleration techniques with controlled aliasing. We were thus able to set up two corresponding, application-oriented whole-brain fMRI protocols at above-average spatial resolution at 3 T. Thanks to the opportunities for time saving that are unique to 3D-EPI, a k -space undersampling factor of only six (3D) compared to a slice acceleration factor of eight (SMS) were required to achieve the same short volume TR of 0.53 s. Accordingly, using 3D-EPI a much reduced SNR penalty was expected, compared to SMS-EPI.

The high temporal resolution was fundamental, since we aimed at minimal probability of cardiac frequency overlap with the typical BOLD frequency range. In fact, prolonging TR to ≥ 0.7 s, e.g. by relaxing the SMS-EPI slice acceleration factor from eight to six (Nyquist frequency ≤ 0.71 Hz), would shift the cardiac alias peak, as observed in the second example PSD shown in Fig. 4, from ~ 0.55 – 0.72 Hz to ~ 0.09 – 0.26 Hz or even below, i.e. the fundamental cardiac frequencies would overlap with (or be very close to) the BOLD frequencies. Furthermore, a likely overlap of the cardiac alias peak with the respiratory peak would impede discriminating the two, which may potentially impact the effectiveness of data “cleaning” approaches based on the GLM (as used here) or on ICA (Salimi-Khorshidi et al., 2014). Even though the frequency separation may not be as critical in general (which is beyond the scope of this work), our findings may thus provide a practical recommendation when investigators aim to minimize the influence of physiological noise on BOLD signal.

The short volume TR suggested the implementation of SPAIR fat suppression into our 3D-EPI as a complementary means to improve robustness of binomial-11 WE. While the combination of binomial-11 WE and SPAIR is not easily applicable, if TR is significantly increased, more effective but slightly longer binomial-121 WE pulses, which are not limited to short TRs, could instead be employed alone. To the best of our knowledge, comparable multiband WE pulses with acceptable slice-profiles are not yet feasible and compatible with RF peak power and SAR limitations (recall that binomial WE requires a pulse spacing of approximately 1.2 ms at 3 T). Therefore, we currently consider CHESS fat saturation (here ~ 12 ms) and relatively long multiband pulses (here ~ 7 ms) as the most limiting factor for SMS-EPI in the context of rapid whole-brain fMRI ($\sim 25\%$ of TR = 530 ms compared to SPAIR and binomial-11 WE, which add up to only $\sim 9\%$ of the 3D-EPI volume TR). Slab-selective 3D-EPI, on the other hand, may require discarding of slices covering the side band of the excited slab, if not included in the fMRI analysis. Due to the k -space based six-fold undersampling, it is difficult to quantify the actual acquisition time for the four slices discarded in the present study (ten excitations would be required regardless of whether 60, 56 or 55 slices were to be reconstructed). However, if six slices were discarded, one excitation would only be performed for the purpose of slice oversampling. This would correspond to approximately 10% of the total volume TR, depending on whether or not semi-elliptical vETL was applied. Conservative slice partial Fourier sampling (e.g. 9/10) could be applied to compensate for the extra time needed for slice oversampling.

We demonstrated essential and exclusive 3D-EPI time savings by applying vETL along 2D phase encode trajectories at above-average spatial resolution at 3 T. Previously, vETL has been utilized to acquire high-resolution 3D-EPI data along 1D phase encode trajectories at 3 and 7 T (Stirnberg et al., 2014). It is noteworthy that, for the present 3D-EPI protocol, the additional duration of one SPAIR module occurring every ten excitations (~ 29 ms $\approx 5\%$ of TR = 530 ms) approximately corresponded to the time saved by applying semi-elliptical vETL (~ 35 ms $\approx 7\%$ of TR = 530 ms). Conversely, with vETL and without SPAIR even a TR of 500 ms could have been achieved at only six-fold k -space undersampling, which is identical to the minimum TR possible using the eight-fold accelerated SMS-EPI. On the

Table 2
Temporal SNR group analysis.

GM ROI	Processing	SMS-EPI	3D-EPI	Ratio	<i>p</i>	<i>T</i>
Cortical	HP	46 (3.9%)	54 (3.6%)	1.18 (5.3%)	$3.7 \cdot 10^{-6}$	9.9
	HP, M	52 (3.7%)	59 (3.1%)	1.23 (4.8%)	$9.3 \cdot 10^{-8}$	15.3
	HP, M, N	51 (3.6%)	64 (2.8%)	1.27 (4.6%)	$2.3 \cdot 10^{-9}$	23.3
	BP	118 (5.8%)	126 (7.1%)	1.07 (9.1%)	$1.3 \cdot 10^{-1}$ (#)	1.7
	BP, M	164 (5.2%)	190 (5.2%)	1.16 (7.3%)	$2.3 \cdot 10^{-4}$	5.9
	BP, M, N	200 (4.8%)	241 (4.0%)	1.21 (6.2%)	$1.1 \cdot 10^{-5}$	8.8
	Subcortical	HP	20 (3.1%)	30 (2.9%)	1.50 (4.3%)	$4.9 \cdot 10^{-9}$
HP, M		20 (3.1%)	31 (2.8%)	1.54 (4.2%)	$2.0 \cdot 10^{-9}$	23.7
HP, M, N		21 (3.1%)	33 (2.7%)	1.57 (4.1%)	$6.8 \cdot 10^{-10}$	26.8
BP		67 (3.7%)	88 (5.4%)	1.32 (6.5%)	$1.8 \cdot 10^{-4}$	6.1
BP, M		88 (3.4%)	128 (3.5%)	1.45 (4.9%)	$1.8 \cdot 10^{-7}$	14.2
BP, M, N		104 (3.3%)	156 (2.8%)	1.50 (4.3%)	$5.6 \cdot 10^{-9}$	21.1
Cerebellar		HP	36 (3.3%)	49 (4.3%)	1.34 (5.5%)	$4.0 \cdot 10^{-6}$
	HP, M	38 (3.2%)	52 (3.6%)	1.39 (4.9%)	$5.2 \cdot 10^{-7}$	12.6
	HP, M, N	39 (3.2%)	55 (3.7%)	1.41 (4.9%)	$5.9 \cdot 10^{-7}$	12.4
	BP	111 (4.4%)	136 (6.5%)	1.22 (7.9%)	$8.3 \cdot 10^{-4}$	4.9
	BP, M	152 (4.0%)	201 (4.5%)	1.32 (6.0%)	$1.7 \cdot 10^{-6}$	11.0
	BP, M, N	182 (3.4%)	246 (4.1%)	1.35 (5.4%)	$6.8 \cdot 10^{-7}$	12.2

other hand, the numerical phantom simulations in preparation of this study (cf. Fig. 2) indicate that the extra longitudinal relaxation period between volume acquisitions along with SPAIR, recovers the 3% signal loss encountered when only using vETL (reduced average TR across excitations). In fact, the average TR across excitations with SPAIR and vETL almost corresponds to the TR per excitation without SPAIR and constant ETL. Hence, the same tSNR can be expected, albeit with the benefit of more robust fat suppression.

The PSDs in Fig. 4 suggest that, for both EPI protocols, data “cleaning” via motion regression primarily reduces the respiratory peak while additional nuisance regression effectively removes the cardiac peak. In both cases, low-frequency signals attributed to the regressors are reduced as well. Note that a constant (thermal) noise floor remains prevalent across all frequencies that pass the temporal filter, irrespective of nuisance and/or motion regression. The group average maps of relative tSNR increase in Fig. 5 indicate that motion regression primarily affects the edge voxels of the brain, where most contrast changes driven by respiration-induced motion combined with partial voluming are in deed expected. In case of BP filtering, there is a nearly constant tSNR increase across WM, as opposed to HP filtering. Irrespective of the temporal filter, simultaneous motion and nuisance regression apparently results in largest tSNR increases in GM voxels, edge voxels and voxels that can be assigned to major blood vessels. This is observed for both protocols, while generally the tSNR increase by data “cleaning” is clearly stronger for the 3D protocol. Largest tSNR increases are observed for BP-filtered data, which can be explained by the increased impact of reducing the low-frequency physiological noise components relative to the small thermal noise fraction that has passed the temporal filter.

The increased benefit of 3D-EPI from data “cleaning” may be

explained by the inherently increased sensitivity of 3D-EPI to physiological noise (Triantafyllou et al., 2005), even with considerable parallel imaging acceleration (Triantafyllou et al., 2011). Hence, physiological noise removal by RETROICOR, for instance, can have larger effects on 3D-EPI data than on conventional 2D-EPI, as previously shown on the example of high-resolution fMRI at 3 T (Lutti et al., 2013). It is known that physiological noise in 3D-EPI may be reduced by smaller segmentation factors (Van Der Zwaag et al., 2012). However, ten excitations per volume, as used here, already corresponds to the minimum segmentation possible at the given TE, matrix size and undersampling pattern. Nevertheless, the 3D protocol still corresponds to a segmented acquisition as opposed to the SMS protocol. Hence, the effect of improvement by nuisance and motion regression is larger for 3D than for SMS.

The most distinct absolute tSNR advantage of 3D over SMS is located in WM regions in the center of the brain, where tSNR is up to twice as large in 3D compared to tSNR in SMS (Fig. 5). This primarily affects WM, subcortical and cerebellar GM and is most likely a result of both the reduced g-factor and the different T₁ contrast of SMS-EPI and 3D-EPI. This is supported by Fig. 6, which shows, first, a similar but more clearly defined central tSNR benefit of the six-fold over the eight-fold accelerated SMS-EPI (primarily different g-factors, comparable tissue contrast). Second, Fig. 6 D indicates a homogeneous tSNR benefit of about 25% throughout WM with 3D-EPI over SMS-EPI, if both sequences are accelerated by a factor of six (primarily different T₁ contrast, comparable g-factors). Notably, tSNR in GM is approximately equivalent in the case of matched acceleration factors (3D may have ~14% increased sensitivity, though, due to 30% more volumes per unit time). Using the TR-matched protocols, as Fig. 7 and Table 2 show, also in cortical GM regions 3D-tSNR clearly supersedes SMS-tSNR. This becomes particularly clear, if motion and nuisance regression has been employed and if temporal HP filtered data are preferred over temporal BP filtered data. According to the paired T-test (cf. Table 2) the observed tSNR benefit with 3D is highly significant ($p < 0.001$) in all ROIs, except for cortical GM after BP filtering without nuisance or motion regression (cf. Fig. 7 D).

The 3D-EPI acquisition results in higher functional connectivity estimates as compared to the SMS-EPI acquisition. Given that we acquired resting-state data for only ten minutes, which is not sufficient to reach a ceiling value, higher values are favored (Birn et al., 2013). Using very fast sequences for functional connectivity analysis may require higher-order autoregressive models to account for increased temporal autocorrelation (Arbabshirani et al., 2014). However, we do not expect differences with this regard between SMS-EPI and 3D-EPI, if both are TR- and TE-matched, since individual volumes are self-contained in either case. The ICC maps displayed in Fig. 9 next to the corresponding connectivity maps represent a rough, spatially resolved measure for test/retest reliability. ICCs are defined as the ratio of between-subjects divided by within-subjects variance. Both large intra-individual differences and low test/retest variance increase the ICCs. The fact that the ICC maps match the mean connectivity maps is therefore non-trivial. It indicates that reliability is high in places where connectivity is high and intra-individual differences are meaningful. The ICCs appear to favor 3D-EPI for the motor and default-network, while the ICCs are rather similar for the visual network. The increased functional connectivity estimates suggest that the total scan time of a corresponding 3D-EPI resting state fMRI protocol may be reduced, compared to SMS-EPI, while maintaining identical statistical power. Reducing acquisition time is especially attractive for large cohort studies, as it leaves opportunity for other scans (Breteler et al., 2014; Miller et al., 2016). Higher sensitivity and reliability are also vital in large cohort studies, as variance across individuals and across longitudinal visits, are the primary signal. In contrast, when testing a specific hypothesis, the 3D-EPI protocol may allow for smaller groups than the SMS-EPI protocol.

The time-efficient 3D-EPI sequence allowed for less “aggressive”

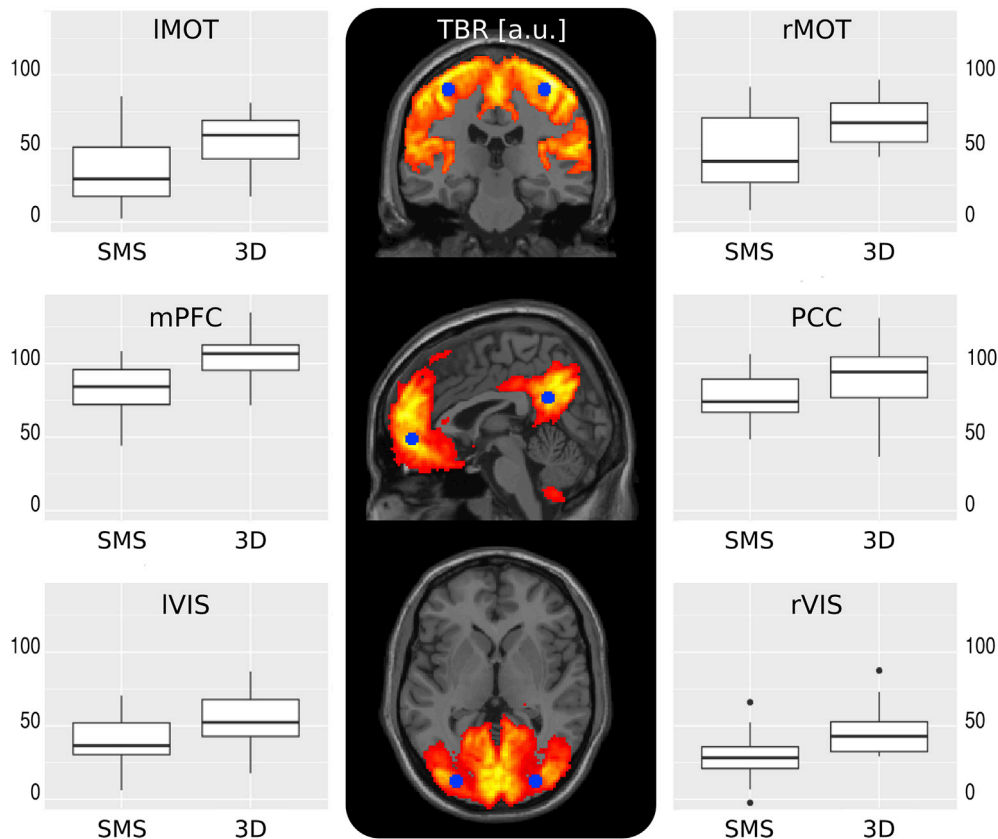


Fig. 8. Region-of-interest (ROI) analyses of functional connectivity for each sequence (SMS/3D) averaged over both sessions (test/retest) for the motor (top), default (middle) and visual (bottom) network. Blue markers indicate the ROIs used for quantitative connectivity analyses. The activity map is only shown for illustrative purposes to appreciate the locations of the ROIs. The box plots compare the distribution of connectivity estimates by sequence type separately for left (l) and right (r) motor (MOT) and visual (VIS) cortex as well as posterior cingulate cortex (PCC) and medial prefrontal cortex (mPFC). The ANOVA results stated in the text refer to the average connectivity of the two ROIs per network.

k-space undersampling to achieve the same short TR as with a corresponding SMS-EPI protocol. As a consequence, we found a significant tSNR benefit throughout the brain, in particular in central brain regions that often suffer from strong *g*-factor increases, if high slice acceleration factors are applied. This resulted in stronger functional connectivity measures for several standard networks – not only, but in particular after motion and nuisance regression is performed to remove physiological noise. Although we presented results for potentially “overfitted” noise regressions, we found similar results with six motion regressors and/or “only” RETROICOR and RVHCOR. Relaxing the TR-constraint slightly would have allowed us to use an SMS-EPI protocol with a slice acceleration factor of seven ($TR_{\min} = 560$ ms for 56 slices), whereas the 3D-EPI protocol would have remained unchanged, besides a slightly relaxed average TR across excitations ($TR_{\min} = 580$ ms/630 ms for 55/60 slices using an acceleration factor of five). However, extrapolating from the tSNR ratio maps for matching acceleration factors of six (cf. Fig. 6 D), which indicates only a tSNR benefit of SMS-EPI over 3D-EPI in CSF, we would expect similar results with respect to tSNR and functional connectivity, though not that strongly differing between SMS-EPI and 3D-EPI in cerebellar and subcortical GM. We emphasize that our SMS and 3D data quality depended on a dedicated slice-GRAPPA reconstruction, on the one hand, and a generic CAIPIRINHA reconstruction, on the other hand, which has explicitly been accepted for applicability under realistic conditions (on-line image reconstruction). Changing reconstruction approaches or parameters might influence the findings. Sequence details, such as the CAIPIRINHA or slice-GRAPPA ACS acquisition method, can also have significant impact on 3D-EPI and SMS-EPI tSNR (Vu et al., 2014, Ivanov et al. (2015), Talagala et al. (2016)) and across-run variability (Blazejewska et al., 2017). While we have tailored our custom 3D-EPI sequence to

maximize tSNR, we relied on an optimal SMS-EPI implementation by the vendor. We also note that the EPI protocols compared here were optimized for a high-end commercial scanner with powerful gradients and a 52-channel head receive array, which allowed for relatively “aggressive” acceleration. This might limit translation of our protocol to scanners with weaker gradients or fewer receive coils. However, the underlying idea to utilize exclusive volumetric acceleration techniques complementary to parallel imaging, can be translated with ease. This includes cases, which are per se not compatible with parallel imaging principles. Combined, slice partial Fourier sampling (up to 12.5–37.5% TR reduction), rapid water excitation, instead of fat saturation (up to 20% TR reduction and global tSNR increase (Stirnberg et al., 2016a)), and variable echo train lengths (up to 10% TR reduction with semi-elliptical sampling) may result in considerable tSNR- and BOLD-sensitivity benefits, even if no, or only moderate parallel imaging-based acceleration can be employed. In either case, our findings show it is important to consider corrections for physiological noise when developing, or optimizing, a 3D- or SMS-EPI protocol.

5. Conclusion

Rapid whole-brain 3D-EPI has significant advantages over SMS-EPI when using additional dedicated techniques to boost acquisition efficiency. Some beneficial techniques are exclusively available to 3D-EPI, including variable echo train lengths, fast water excitation and slice partial Fourier sampling. Our results suggest that optimally acquired 3D-EPI data benefits considerably more from motion and nuisance regression than SMS-EPI data. The analytic SNR advantage, as a result of less *k*-space undersampling, is hence even more pronounced. Consequently, our optimized 3D-EPI sequence has improved sensitivity in functional

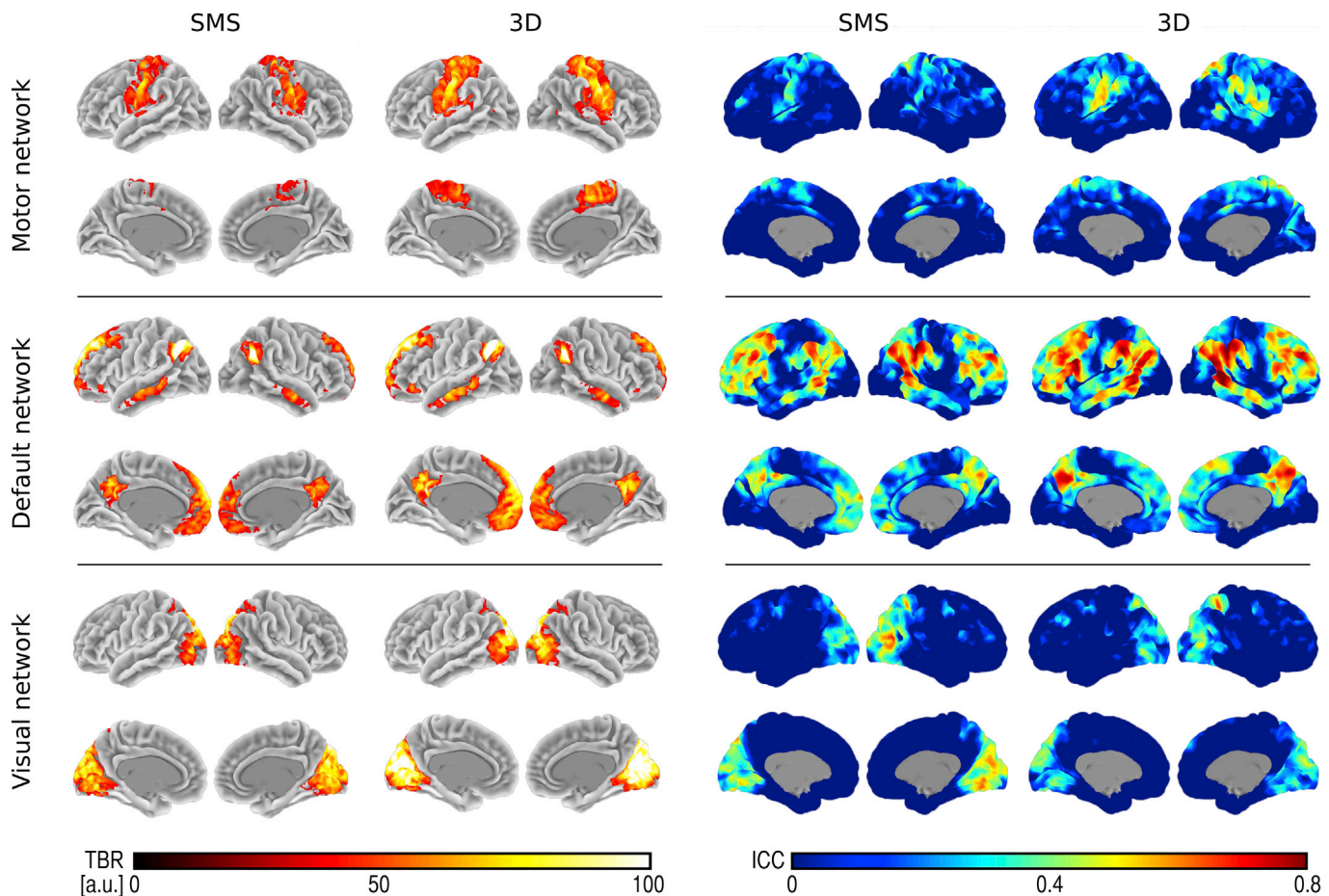


Fig. 9. Cortical surface maps of average functional connectivity on the left and ICC maps indicating test/retest reliability on the right. Each side shows estimates for the left and right hemisphere and midline, separated by sequence type for the motor (top), default (middle) and visual (bottom) network.

connectivity analyses compared to SMS-EPI. This benefit of 3D-EPI is expected to become even more apparent at higher field strengths.

Acknowledgements

RS gratefully thanks Eberhard D. Pracht for his broad nitype support and Philipp Ehse for valuable comments and suggestions.

References

- Arbabshirani, M.R., Damaraju, E., Phlypo, R., Plis, S., Allen, E., Ma, S., Mathalon, D., Preda, A., Vaidya, J.G., Adali, T., Calhoun, V.D., 2014. Impact of autocorrelation on functional connectivity. *Neuroimage* 102, 294–308. <http://dx.doi.org/10.1016/j.neuroimage.2014.07.045>.
- Beckmann, C.F., Smith, S.M., 2005. Tensorial extensions of independent component analysis for multisubject fMRI analysis. *Neuroimage* 25, 294–311. <http://dx.doi.org/10.1016/j.neuroimage.2004.10.043>.
- Bennett, C.M., Miller, M.B., 2010. How reliable are the results from functional magnetic resonance imaging? *Ann. N. Y. Acad. Sci.* 1191, 133–155. <http://dx.doi.org/10.1111/j.1749-6632.2010.05446.x>.
- Bernstein, M.A., Fain, S.B., Riederer, S.J., 2001. Effect of windowing and zero-filled reconstruction of MRI data on spatial resolution and acquisition strategy. *J. Magn. Reson. Imaging* 14, 270–280. <http://dx.doi.org/10.1002/jmri.1183>.
- Bhat, H., Polimeni, J.R., Cauley, S.F., Setsompop, K., Wald, L.L., Heberlein, K., 2014. Motion insensitive ACS acquisition method for in-plane and simultaneous multi-slice accelerated EPI. In: *Proc. Intl. Soc. Mag. Reson. Med.*, vol. 22, p. 644.
- Birn, R.M., Molloy, E.K., Patriat, R., Parker, T., Meier, T.B., Kirk, G.R., Nair, V.A., Meyerand, M.E., Prabhakaran, V., 2013. The effect of scan length on the reliability of resting-state fMRI connectivity estimates. *Neuroimage* 83, 550–558. <http://dx.doi.org/10.1016/j.neuroimage.2013.05.099>.
- Birn, R.M., Smith, M.A., Jones, T.B., Bandettini, P.A., 2008. The respiration response function: the temporal dynamics of fMRI signal fluctuations related to changes in respiration. *Neuroimage* 40, 644–654. <http://dx.doi.org/10.1016/j.neuroimage.2007.11.059>.
- Blaziejewska, A.I., Bhat, H., Wald, L.L., Polimeni, J.R., 2017. Reduction of across-run variability of temporal SNR in accelerated EPI time-series data through FLEET-based robust autocalibration. *Neuroimage* 152, 348–359. <http://dx.doi.org/10.1016/j.neuroimage.2017.02.029>.
- Brenner, D., Stirnberg, R., Pracht, E.D., Stöcker, T., 2014. Two-dimensional accelerated MP-RAGE imaging with flexible linear reordering. *Magn. Reson. Mater. Phys. Biol. Med.* 27, 455–462. <http://dx.doi.org/10.1007/s10334-014-0430-y>.
- Breteler, M.M., Stöcker, T., Pracht, E., Brenner, D., Stirnberg, R., 2014. MRI in the rhineland study: a novel protocol for population neuroimaging. *Alzheimer's Dement.* 10, P92. <http://dx.doi.org/10.1016/j.jalz.2014.05.172>.
- Breuer, F.A., Blaimer, M., Mueller, M.F., Seiberlich, N., Heidemann, R.M., Griswold, M.A., Jakob, P.M., 2006. Controlled aliasing in volumetric parallel imaging (2D CAIPRINHA). *Magn. Reson. Med.* 55, 549–556. <http://dx.doi.org/10.1002/mrm.20787>.
- Bydder, G.M., Pennock, J.M., Steiner, R.E., Khenia, S., Payne, J.A., Young, I.R., 1985. The short TI inversion recovery sequence—An approach to MR imaging of the abdomen. *Magn. Reson. Imaging* 3, 251–254. [http://dx.doi.org/10.1016/0730-725X\(85\)90354-6](http://dx.doi.org/10.1016/0730-725X(85)90354-6).
- Cauley, S.F., Polimeni, J.R., Bhat, H., Wald, L.L., Setsompop, K., 2014. Interslice leakage artifact reduction technique for simultaneous multislice acquisitions. *Magn. Reson. Med.* 72, 93–102. <http://dx.doi.org/10.1002/mrm.24898>.
- Chang, C., Cunningham, J.P., Glover, G.H., 2009. Influence of heart rate on the BOLD signal: the cardiac response function. *Neuroimage* 44, 857–869. <http://dx.doi.org/10.1016/j.neuroimage.2008.09.029>.
- Glover, G.H., Li, T.Q., Ress, D., 2000. Image-based method for retrospective correction of physiological motion effects in fMRI: RETROICOR. *Magn. Reson. Med.* 44, 162–167. [http://dx.doi.org/10.1002/1522-2594\(200007\)44:1<162::AID-MRM23>3.0.CO;2-E](http://dx.doi.org/10.1002/1522-2594(200007)44:1<162::AID-MRM23>3.0.CO;2-E).
- Gorgolewski, K., Burns, C.D., Madison, C., Clark, D., Halchenko, Y.O., Waskom, M.L., Ghosh, S.S., 2011. Nipype: a flexible, lightweight and extensible neuroimaging data processing framework in python. *Front. Neuroinform* 5, 13. <http://dx.doi.org/10.3389/fninf.2011.00013>.
- Griswold, M.A., Jakob, P.M., Heidemann, R.M., Nittka, M., Jellus, V., Wang, J., Kiefer, B., Haase, A., 2002. Generalized autocalibrating partially parallel acquisitions (GRAPPA). *Magn. Reson. Med.* 47, 1202–1210. <http://dx.doi.org/10.1002/mrm.10171>.
- Haase, A., Frahm, J., Hänicke, W., Matthaei, D., 1985. 1H NMR chemical shift selective (CHESS) imaging. *Phys. Med. Biol.* 30, 341–344. <http://dx.doi.org/10.1088/0031-9155/30/4/008>.

- Hallquist, M.N., Hwang, K., Luna, B., 2013. The nuisance of nuisance regression: spectral misspecification in a common approach to resting-state fMRI preprocessing reintroduces noise and obscures functional connectivity. *Neuroimage* 82, 208–225. <http://dx.doi.org/10.1016/j.neuroimage.2013.05.116>.
- Hennig, J., 1991a. Echoes—how to generate, recognize, use or avoid them in MR-imaging sequences. Part I: fundamental and not so fundamental properties of spin echoes. *Concepts Magn. Reson* 3, 125–143. <http://dx.doi.org/10.1002/cmr.1820030302>.
- Hennig, J., 1991b. Echoes—how to generate, recognize, use or avoid them in MR-imaging sequences. Part II: echoes in imaging sequences. *Concepts Magn. Reson* 3, 179–192. <http://dx.doi.org/10.1002/cmr.1820030402>.
- Hore, P.J., 1983. Solvent suppression in fourier transform nuclear magnetic resonance. *J. Magn. Reson* 55, 283–300. [http://dx.doi.org/10.1016/0022-2364\(83\)90240-8](http://dx.doi.org/10.1016/0022-2364(83)90240-8).
- Ivanov, D., Barth, M., Uludağ, K., Poser, B.A., 2015. Robust ACS acquisition for 3D echo planar imaging. In: *Proc. Int. Soc. Magn. Reson. Med.*, p. 2059. <http://dx.doi.org/10.1002/jmri.24551>.
- Jenkinson, M., Beckmann, C.F., Behrens, T.E.J., Woolrich, M.W., Smith, S.M., 2012. Fsl. *Neuroimage* 62, 782–790. <http://dx.doi.org/10.1016/j.neuroimage.2011.09.015>.
- Larkman, D.J., Hajnal, J.V., Herlihy, A.H., Coutts, G.A., Young, I.R., Ehnholm, G., 2001. Use of multicoil arrays for separation of signal from multiple slices simultaneously excited. *J. Magn. Reson. Imaging* 13, 313–317. [http://dx.doi.org/10.1002/1522-2586\(200102\)13:2<313::AID-JMRI1045>3.0.CO;2-W](http://dx.doi.org/10.1002/1522-2586(200102)13:2<313::AID-JMRI1045>3.0.CO;2-W).
- Lutti, A., Thomas, D.L., Hutton, C., Weiskopf, N., 2013. High-resolution functional MRI at 3 T: 3D/2D echo-planar imaging with optimized physiological noise correction. *Magn. Reson. Med.* 69, 1657–1664. <http://dx.doi.org/10.1002/mrm.24398>.
- Mansfield, P., Howsemann, A.M., Ordidge, R.J., 1989. Volumar imaging using NMR spin echoes: echo-volumar imaging (EVI) at 0.1 T. *J. Phys. E* 22, 324–330. <http://dx.doi.org/10.1088/0022-3735/22/5/012>.
- Miller, K.L., Alfaro-Almagro, F., Bangerter, N.K., Thomas, D.L., Yacoub, E., Xu, J., Bartsch, A.J., Jbabdi, S., Sotiropoulos, S.N., Andersson, J.L.R., Griffanti, L., Douaud, G., Okell, T.W., Weale, P., Dragonu, I., Garratt, S., Hudson, S., Collins, R., Jenkinson, M., Matthews, P.M., Smith, S.M., 2016. Multimodal population brain imaging in the UK Biobank prospective epidemiological study. *Nat. Neurosci.* 19, 1523–1536. <http://dx.doi.org/10.1038/nn.4393>.
- Millman, K.J., Brett, M., 2007. Analysis of functional magnetic resonance imaging in Python. *Comput. Sci. Eng.* 9, 52–55. <http://dx.doi.org/10.1109/Mcse.2007.46>.
- Mugler, J.P., Brookeman, J.R., 1990. Three-dimensional magnetization-prepared rapid gradient-echo imaging (3D MP RAGE). *Magn. Reson. Med.* 15, 152–157. <http://dx.doi.org/10.1002/mrm.1910150117>.
- Narsude, M., Gallichan, D., Van Der Zwaag, W., Gruetter, R., Marques, J.P., 2016. Three-dimensional echo planar imaging with controlled aliasing: a sequence for high temporal resolution functional MRI. *Magn. Reson. Med.* 75, 2350–2361. <http://dx.doi.org/10.1002/mrm.25835>.
- Narsude, M., Marques, J.P., Gallichan, D., Gruetter, R., 2013. Superior GRAPPA reconstruction with reduced g-factor noise using 2D CAIPIRINHA for 3D EPI. In: *Proc. Int. Soc. Magn. Reson. Med.*, p. 3705.
- Narsude, M., Van Der Zwaag, W., Kober, T., Gruetter, R., Marques, J.P., 2014a. Improved temporal resolution for functional studies with reduced number of segments with three-dimensional echo planar imaging. *Magn. Reson. Med.* 72, 786–792. <http://dx.doi.org/10.1002/mrm.24975>.
- Narsude, M., Zwaag, W., van der Gallichan, D., Gruetter, R., Marques, J., 2014b. Resting state networks detection, the importance of high temporal resolution: a comparison study between 2D-EPI, SMS 2D-EPI and 3D-EPI-CAIPI acquisitions. In: *Proc. Int. Soc. Magn. Reson. Med.*, p. 4325. <http://dx.doi.org/10.1002/mrm.24975>.
- Olipiant, T.E., 2007. Python for scientific computing. *Comput. Sci. Eng.* 9, 10–20. <http://dx.doi.org/10.1109/MCSE.2007.58>.
- O'Brien, K.R., Kober, T., Haggmann, P., Maeder, P., Marques, J., Lazeyras, F., Krueger, G., Roche, A., 2014. Robust T1-weighted structural brain imaging and morphometry at 7T using MP2RAGE. *PLoS One* 9. <http://dx.doi.org/10.1371/journal.pone.0099676>.
- Poser, B., Kemper, V., Ivanov, D., Kannengiesser, S., Uludağ, K., Barth, M., 2013. CAIPIRINHA-accelerated 3D EPI for high temporal and/or spatial resolution EPI acquisitions. In: *Magn. Reson. Mater. Physics, Biol. Med.*, pp. 151–301. <http://dx.doi.org/10.1007/s10334-013-0383-6>.
- Poser, B., Koopmans, P., Witzel, T., Wald, L., Barth, M., 2010. Three dimensional echo-planar imaging at 7 Tesla. *Neuroimage* 51, 261–266. <http://dx.doi.org/10.1016/j.neuroimage.2010.01.108>.
- Poser, B.A., Ivanov, D., Kannengiesser, S.A., Uludağ, K., Barth, M., 2014. Accelerated 3D EPI using 2D blipped-CAIPI for high temporal and/or spatial resolution. In: *Proc. Int. Soc. Magn. Reson. Med.*, p. 1506.
- Power, J.D., Mitra, A., Laumann, T.O., Snyder, A.Z., Schlaggar, B.L., Petersen, S.E., 2014. Methods to detect, characterize, and remove motion artifact in resting state fMRI. *Neuroimage* 84, 320–341. <http://dx.doi.org/10.1016/j.neuroimage.2013.08.048>.
- Salimi-Khorshidi, G., Douaud, G., Beckmann, C.F., Glasser, M.F., Griffanti, L., Smith, S.M., 2014. Automatic denoising of functional MRI data: combining independent component analysis and hierarchical fusion of classifiers. *Neuroimage* 90, 449–468. <http://dx.doi.org/10.1016/j.neuroimage.2013.11.046>.
- Schultz, A.P., Chhatwal, J.P., Huijbers, W., Hedden, T., Dijk, K.R.A., van, McLaren, D.G., Ward, A.M., Wigman, S., Sperling, R.A., 2014. Template based rotation: a method for functional connectivity analysis with a priori templates. *Neuroimage* 102, 620–636. <http://dx.doi.org/10.1016/j.neuroimage.2014.08.022>.
- Setsompop, K., Gagoski, B.A., Polimeni, J.R., Witzel, T., Wedeen, V.J., Wald, L.L., 2012. Blipped-controlled aliasing in parallel imaging for simultaneous multislice echo planar imaging with reduced g-factor penalty. *Magn. Reson. Med.* 67, 1210–1224. <http://dx.doi.org/10.1002/mrm.23097>.
- Shrout, P.E., Fleiss, J.L., 1979. Intraclass correlations: uses in assessing rater reliability. *Psychol. Bull.* 86, 420–428. <http://dx.doi.org/10.1037/0033-2909.86.2.420>.
- Smith, S.M., Beckmann, C.F., Andersson, J., Auerbach, E.J., Bijsterbosch, J., Douaud, G., Duff, E., Feinberg, D.A., Griffanti, L., Harms, M.P., Kelly, M., Laumann, T., Miller, K.L., Moeller, S., Petersen, S., Power, J., Salimi-Khorshidi, G., Snyder, A.Z., Vu, A.T., Woolrich, M.W., Xu, J., Yacoub, E., Ugurbil, K., Van Essen, D.C., Glasser, M.F., 2013. Resting-state fMRI in the human connectome project. *Neuroimage* 80, 144–168. <http://dx.doi.org/10.1016/j.neuroimage.2013.05.039>.
- Sotiropoulos, S.N., Jbabdi, S., Xu, J., Andersson, J.L., Moeller, S., Auerbach, E.J., Glasser, M.F., Hernandez, M., Sapiro, G., Jenkinson, M., Feinberg, D.A., Yacoub, E., Lenglet, C., Van Essen, D.C., Ugurbil, K., Behrens, T.E.J., 2013. Advances in diffusion MRI acquisition and processing in the human connectome project. *Neuroimage* 80, 125–143. <http://dx.doi.org/10.1016/j.neuroimage.2013.05.057>.
- Stirnberg, R., Brenner, D., Stöcker, T., 2014. Variable flip angles and echo train lengths in segmented 3d-EPI at 3 and 7 Tesla. In: *Proc. Int. Soc. Magn. Reson. Med.*, p. 0609.
- Stirnberg, R., Brenner, D., Stöcker, T., Shah, N.J., 2016a. Rapid fat suppression for three-dimensional echo planar imaging with minimized specific absorption rate. *Magn. Reson. Med.* 76, 1517–1523. <http://dx.doi.org/10.1002/mrm.26063>.
- Stirnberg, R., Huijbers, W., Poser, B.A., Stöcker, T., 2016b. Ultra-fast gradient echo EPI with controlled aliasing at 3T: simultaneous multi-slice vs. 3D-EPI. In: *Proc. Int. Soc. Magn. Reson. Med.*
- Stirnberg, R., Pflugfelder, D., Stöcker, T., Shah, N.J., 2013. High-resolution 3D-fMRI at 9.4 Tesla with intrinsically minimised geometric distortions. In: *Proc. Int. Soc. Magn. Reson. Med.*, p. 2372.
- Talagala, S.L., Sarlls, J.E., Liu, S., Inati, S.J., 2016. Improvement of temporal signal-to-noise ratio of GRAPPA accelerated echo planar imaging using a FLASH based calibration scan. *Magn. Reson. Med.* 75, 2362–2371. <http://dx.doi.org/10.1002/mrm.25846>.
- Triantafyllou, C., Hoge, R.D., Krueger, G., Wiggins, C.J., Potthast, A., Wiggins, G.C., Wald, L.L., 2005. Comparison of physiological noise at 1.5 T, 3 T and 7 T and optimization of fMRI acquisition parameters. *Neuroimage* 26, 243–250. <http://dx.doi.org/10.1016/j.neuroimage.2005.01.007>.
- Triantafyllou, C., Polimeni, J.R., Wald, L.L., 2011. Physiological noise and signal-to-noise ratio in fMRI with multi-channel array coils. *Neuroimage* 55, 597–606. <http://dx.doi.org/10.1016/j.neuroimage.2010.11.084>.
- Tse, D.H.Y., Wiggins, C.J., Ivanov, D., Brenner, D., Hoffmann, J., Mirkes, C., Shajan, G., Scheffler, K., Uludağ, K., Poser, B.A., 2016. Volumetric imaging with homogenised excitation and static field at 9.4 T. *Magn. Reson. Mater. Physics, Biol. Med.* 29, 333–345. <http://dx.doi.org/10.1007/s10334-016-0543-6>.
- Ugurbil, K., Xu, J., Auerbach, E.J., Moeller, S., Vu, A.T., Duarte-Carvajalino, J.M., Lenglet, C., Wu, X., Schmitter, S., Van de Moortele, P.F., Strupp, J., Sapiro, G., De Martino, F., Wang, D., Harel, N., Garwood, M., Chen, L., Feinberg, D.A., Smith, S.M., Miller, K.L., Sotiropoulos, S.N., Jbabdi, S., Andersson, J.L.R., Behrens, T.E.J., Glasser, M.F., Van Essen, D.C., Yacoub, E., 2013. Pushing spatial and temporal resolution for functional and diffusion MRI in the Human Connectome Project. *Neuroimage* 80, 80–104. <http://dx.doi.org/10.1016/j.neuroimage.2013.05.012>.
- Van Der Zwaag, W., Marques, J.P., Kober, T., Glover, G., Gruetter, R., Krueger, G., 2012. Temporal SNR characteristics in segmented 3D-EPI at 7T. *Magn. Reson. Med.* 67, 344–352. <http://dx.doi.org/10.1002/mrm.23007>.
- Van Dijk, K.R. a, Hedden, T., Venkataraman, A., Evans, K.C., Lazar, S.W., Buckner, R.L., 2010. Intrinsic functional connectivity as a Tool for human connectomics: Theory, properties, and optimization. *J. Neurophysiol.* 103, 297–321. <http://dx.doi.org/10.1152/jn.00783.2009>.
- Vu, A.T., Moeller, S., Auerbach, E., Ugurbil, K., Yacoub, E., 2014. GRE reference scan for robust reconstruction of high resolution slice and in-plane accelerated 2D GE EPI at 7T. In: *Proc. Intl. Soc. Mag. Reson. Med.*, vol. 22, p. 1414.
- Xu, J., Moeller, S., Auerbach, E.J., Strupp, J., Smith, S.M., Feinberg, D.A., Yacoub, E., Ugurbil, K., 2013. Evaluation of slice accelerations using multiband echo planar imaging at 3T. *Neuroimage* 83, 991–1001. <http://dx.doi.org/10.1016/j.neuroimage.2013.07.055>.
- Zahneisen, B., Ernst, T., Poser, B.A., 2015. SENSE and simultaneous multislice imaging. *Magn. Reson. Med.* 74, 1356–1362. <http://dx.doi.org/10.1002/mrm.25519>.
- Zahneisen, B., Poser, B.A., Ernst, T., Stenger, V.A., 2014. Three-dimensional Fourier encoding of simultaneously excited slices: generalized acquisition and reconstruction framework. *Magn. Reson. Med.* 71, 2071–2081. <http://dx.doi.org/10.1002/mrm.24875>.